Surface oxygen vacancy and graphene quantum dots co-modified Bi_2WO_6 toward highly efficient photocatalytic reduction of CO_2

Shaofeng Xiong [a,*], Shundong Bao [a], Weian Wang [a], Jian Hao [b], Yu Mao [c], Pingle Liu [a,**], Yanping Huang [a], Zhengkang Duan [a], Yang Lv [a], Donghong Ouyang [d]

[a] *College of Chemical Engineering, Xiangtan University, Xiangtan, Hunan 411105, China*
[b] *State Key Laboratory of High-efficiency Utilization of Coal and Green Chemical Engineering, Ningxia University, Yinchuan, Ningxia 750021, China*
[c] *Joint International Center for Carbon-dioxide Capture and Storage (iCCS), Advanced Catalytic Engineering Research Center of the Ministry of Education, College of Chemistry and Chemical Engineering, Hunan University, Changsha 410082, China*
[d] *Xiangtan Sepiolite Technology Co., Ltd., Xiangtan, Hunan 411200, China*

ARTICLE INFO

ABSTRACT

Weak light-harvesting capability and low electron-hole separation efficiency remain significant problems unresolved in the design of high-efficient photocatalyst. This work designed and prepared a surface oxygen vacancy (Vo) and graphene quantum dots (GQDs) co-modified Bi_2WO_6 ($GQDs/BWO_{6-x}$). It exhibited enhanced photocatalytic conversion of CO_2 to CO with a yield of 43.9 $\mu mol \cdot g^{-1} \cdot h^{-1}$, which is 1.7-fold higher than Bi_2WO_6 (BWO). The photogenerated electrons over $GQDs/BWO_{6-x}$ had a longer average fluorescence lifetime (3.3 ns) than BWO (2.7 ns), implying a high electron-hole separation efficiency. The DFT calculation results revealed that the electrons in $GQDs/BWO_{6-x}$ flow from the Vo-remote atoms to the Vo-neighboring atoms instead of confining in the GQDs molecules. Easy transformation of *COOH to *CO, a rate-limiting step, was suggested by an energy barrier calculation result (0.16 eV for $GQDs/BWO_{6-x}$, 1.12 eV for BWO).

1. Introduction

Solar energy-driven conversion of CO_2 into sustainable hydrocarbon fuels is a promising strategy to mitigate the energy crisis and global warming [1]. Fujishima and his coworkers made their pioneering contribution in 1979 to the photocatalytic conversion of CO_2 [2]. The TiO_2, WO_3, and ZnO photocatalysts employed in their work belonged to the conventional type, active only under UV light irradiation. Significant effort has been devoted to the search for highly efficient visible-light-driven photocatalysts. More than a hundred types of photocatalysts have been reported for CO_2 conversion. However, most of these photocatalysts showed limited activity under visible light. As visible light accounts for ~43% of solar energy [3], inefficient use of solar energy presents a significant limitation.

Bi_2WO_6 stands out among many attractive candidate semiconductors owing to its appropriate bandgap (~2.7 eV) and good photostability. However, pure Bi_2WO_6 still confronts poor solar photocatalytic activity

arising from weak light-harvesting capability and low electron-hole separation efficiency. The application of Bi_2WO_6 nowadays mainly focuses on photocatalytic pollution degradation and water splitting. Little attention has been paid to photocatalytic CO_2 reduction. Furthermore, the activities for CO_2 conversion to CO or CH_4 were limited.

Strategies have been explored to overcome barriers, including morphology control [4–6], hetero and hybrid nanostructures [7–10], and oxygen vacancy (Vo) [11–13]. Zhang et al. [7] developed 3D Bi_2MoO_6 microspheres to produce CO (Yield: 41.5 $\mu mol \cdot g^{-1} \cdot h^{-1}$) via the photocatalytic reduction of CO_2. Jo et al. [9] constructed a hybrid heterojunction comprising Bi_2WO_6, reduced graphene oxide, and g-C_3N_4 (BWO/RGO/CN) with a 2D/2D/2D configuration for the transformation of CO_2 to CO and CH_4. Kong et al. [10] prepared carbon quantum dots (CQDs)-decorated ultrathin Bi_2WO_6 nanosheets (UBW) for CO_2 photoreduction over the Vis-NIR broad spectrum, and the optimal CH_4 yield was 7.19 $\mu mol \cdot g^{-1} \cdot h^{-1}$.

Surface oxygen vacancy is a promising method to accelerate charge

---

separation. The introduction of surface Vo can lead to some prominent advantages, such as tuning band structure and modifying surface chemical states [11,12]. Li et al. [13] fabricated three different TiO_2 nanomaterials with the surface, surface/bulk, and bulk oxygen vacancies. TiO_2 with surface oxygen vacancies exhibited the highest CH_4 yield of 8.89 ppm·g^{-1}·h^{-1} among three TiO_2 nanomaterials under visible light irradiation. The CH_4 yield of TiO_2 with body oxygen vacancies is the lowest because the bulk oxygen vacancies acted as a recombination center of the charge carriers. Liang et al. [14] designed a hollow Vo-rich g-C_3N_4@CeO_2 photocatalyst, which showed the highest yields of CO (16.8 μmol·g^{-1}). Zhang et al. [15] synthesized oxygen-deficient Bi_2WO_6 by zirconium doping, which exhibited a remarkably enhanced photoactivity toward the degradation of organics than Vo-free Bi_2WO_6. In summary, Vo possesses many prominent advantages in accelerating the charge separation and activation of the reactants. However, the CO yield of the reported Vo-based photocatalysts is still limited. Meanwhile, the Vo's roles in promoting electron-hole separation, tuning band structure, and changing surface chemical states are not understood thoroughly. Furthermore, many works have ignored determining the origin of gas products via the $^{13}CO_2$ isotope labeling measurement, leading to the overestimated yield.

In this study, a GQDs decorated, and Vo-containing Bi_2WO_6 composite (GQDs/BWO_{6-x}) was prepared and used for photocatalytic reduction of CO_2. GQDs are a new class of zero-dimensional (0D) nanomaterials, which are excellent in transferring electrons. In addition, GQDs have unique properties, including excellent photostability, non-toxicity, and superior electronic properties [16]. Therefore, GQDs are supposed to be a hopeful promoter for the composites. To the best of our knowledge, this is the first study that reports a GQDs-based and surface Vo-decorated composite for CO_2 photoreduction under visible light irradiation. We believe that the findings from this work could unveil some insights into the design and development of highly active photocatalysts.

2. Experimental

2.1. Catalyst preparation

2.1.1. Synthesis of GQDs

The procedure for preparing the precursors of GQDs follows the method proposed by Bao et al. [17] and elucidated in our previous work [18]. This procedure includes the preparation of graphene oxide (GO) through a pressurized oxidation method using reduced graphene oxide (rGO) as a precursor and further reducing GO to rGO by ammonia and hydrazine. Typically, 0.05 g of rGO, 6.7 mL HNO_3 (65%, v/v), and 20 mL H_2SO_4 (98%, v/v) were mixed and refluxed at 120 °C for 24 h. The above solution was then cooled down, and neutralized with Na_2CO_3 to pH 7–8. Supernatant liquids were further collected by centrifuging, followed by dialysis through a dialysis bag (USA Viskase Membra-Cel: MD44-3.5 ×500, MWCO: 3500), to obtain purified GQDs solution. Average size of GQDs was controlled by varying the reflux temperature (100–125 °C) and the initial concentration of rGO solution.

2.1.2. Synthesis of GQDs/BWO and pure Bi_2WO_6

GQDs/BWO was prepared by a microwave-hydrothermal method. Typically, 0.165 g of Na_2WO_4.$2H_2O$ and GQDs in various ratios (the typical loading amount of GQDs was 3 wt% of BWO) were dissolved in DI water, followed by sonication for 30 min 0.026 g of cetyl trimethyl ammonium bromide (CTAB) used as a template were added with 0.485 g of $Bi(NO_3)_3$.$5H_2O$ into the above solution under stirring to form the precursor solution. The solution was then poured into a Teflon vessel of a microwave reactor (StartSYNTH Microwave Synthesis Labstation, Milestone, Italy), followed by sealing the vessel with a Teflon cap. The microwave reactor was operated at 120–160 °C for 1.5–3 h. After the reaction, the precipitates were centrifuged and washed three times with DI water and ethanol to remove residual CTAB before drying in a

vacuum chamber at 50 °C for 12 h. The resultant material was denoted as GQDs/BWO.

Pure Bi_2WO_6 was prepared according to the above microwave-assisted hydrothermal procedure except no addition of GQDs.

2.1.3. Synthesis of GQDs/BWO_{6-x}

The preparation of GQDs/BWO_{6-x} followed an alkali etching method [19], as shown in Fig. 1a. Typically, a certain amount of GQDs/BWO was added into a beaker with 0.1 M NaOH, followed by stirring for a certain period of time (1–2 h) at 60 °C. The etched solids were then washed with DI water for four times, before drying for 4 h at 25 °C. The resultant powders were denoted as GQDs/BWO_{6-x}. Vo-contained BWO (BWO_{6-x}) was synthesized according to the same method, except that BWO was used as the starting material instead of GQDs/BWO.

2.2. Morphological and spectroscopic characterization

Powder X-ray diffraction (XRD) pattern was obtained in the 2θ range 5–90° using a Rigaku D/MAX-3C instrument with CuKα source (λ = 0.1541 nm). Morphology and crystal face information were obtained by transmission electron microscopy (TEM, JEM-2100F, 200 kV accelerating voltage) and scanning electron microscopy (SEM, Hitachi JSM-636, 1–30 kV accelerating voltage). Surface electronic states were analyzed by XPS (Escalab 250XI, ThermoFisher). All binding energies were calibrated by using the contaminant carbon (C 1 s = 284.7 eV) as a reference. Fourier transform infrared (FTIR) spectra were measured on a Tensor 27 FTIR spectrometer (Bruker). Diffuse reflectance spectra (DRS) were obtained using a Shimadzu UV-2550 UV–vis–NIR (ultra-violet–visible-near-infrared) spectrophotometer. $BaSO_4$ was used as the standard reflectance material. The bandgap (E_g) of photocatalysts was estimated according to the equation of α$h\nu$=A($h\nu$-E_g)$^{n/2}$ [20]. In this equation, $h\nu$ is the energy of photons, A is a proportional constant, and α is the coefficient of light absorption. n is correlated to the type of semiconductors, which is 4 for an indirect semiconductor and 1 for a direct semiconductor [19]. Because Bi_2WO_6 is a direct semiconductor, the value of 1 was adopted for n in the present instance. Eg of pristine Bi_2WO_6 and GQDs/BWO composite were identified by plotting the correlated values of ($h\nu$-E_g)$^{n/2}$ vs. $h\nu$, and finding the intercepts of the tangents to the plots. Surface photovoltage spectroscopy (SPS) (CEL-SPS1000, Education Au-Light, China) was applied to photoelectric property measurements. Photoluminescence (PL) spectra were recorded by a LS55 spectrofluorometer. Transient photocurrent responses (*i-t*) and electrochemical impedance spectroscopy (EIS) were measured in a quartz cell with a conventional three-electrode system on an electrochemical workstation (Princeton, V3, US).

UV absorbance spectrum of liquid material was recorded on a METASH UV-6100 spectrophotometer. Infrared absorption spectra of solid samples were recorded on a NICOLET 380 FT-IR spectrophotometer using the KBr disk method. Electron paramagnetic resonance (EPR) measurements were performed at liquid nitrogen temperature (77 K) on an EPR spectrometer (Bruker E580).

In situ Fourier transform infrared (FT-IR) spectra were measured in N_2 and CO_2 by a MCT detector (Nicolet iS10). Humid CO_2 was injected into the IR chamber to simulate the actual experimental procedure for bubbling CO_2 into the solution with a sacrificial agent. Photoluminescence spectra decay curves were obtained by using a Hamamatsu instrument (Hamamatsu C5680, Japan), and the corresponding parameters can refer to Wang's work [21].

2.3. Photocatalytic reactions of CO_2 reduction

Photocatalytic activities were studied in a 200 mL Labsolar-III reactor (PerfectLight Company, Beijing, China) with an optical quartz window at the top. A 300 W of Xenon-arc lamp with a 420 nm filter (PLS-SXE300C, Beijing Perfectlight Co. Ltd, China) was positioned ~10 cm above the reactor. In a typical process, 100 mg of the
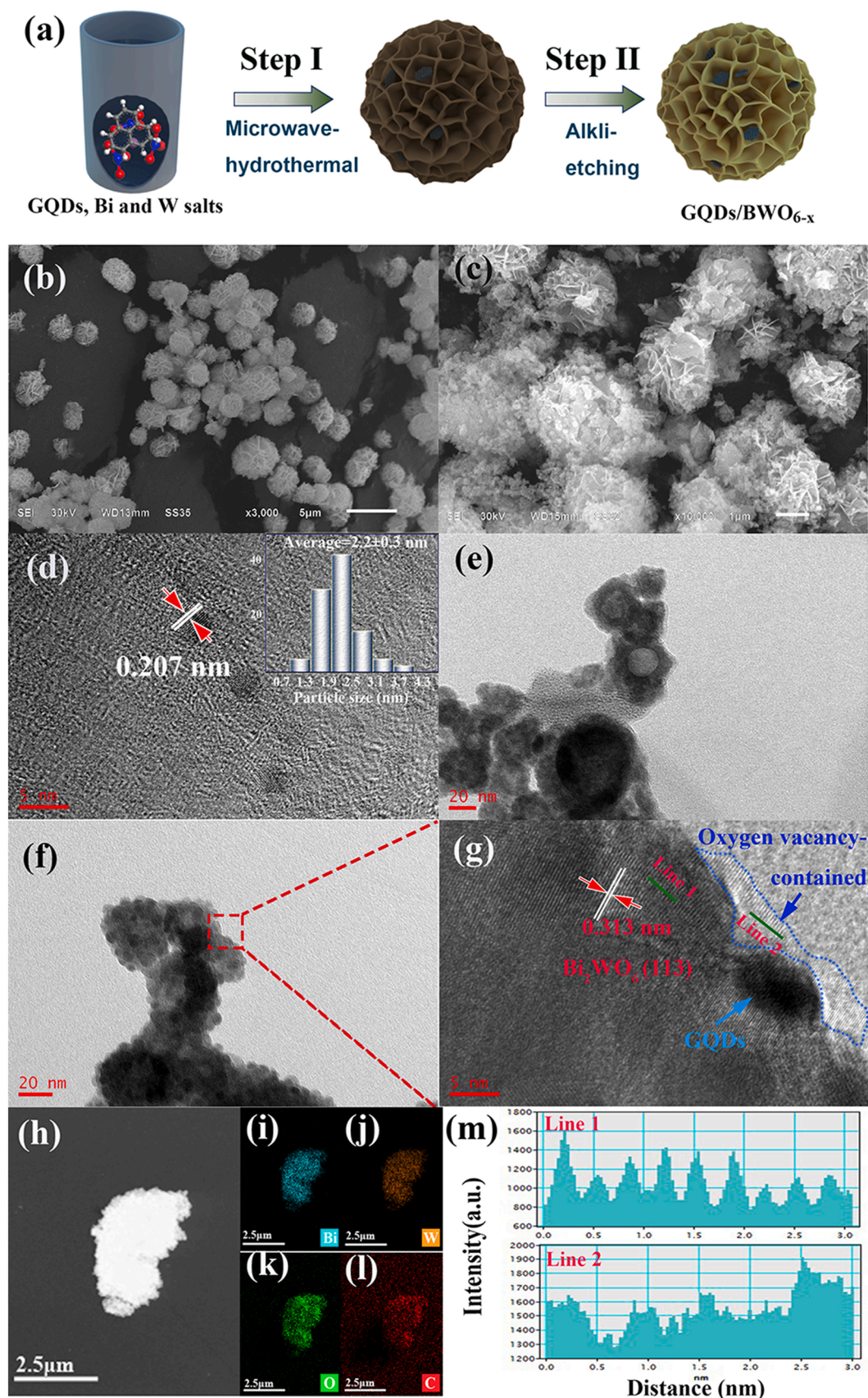
Fig. 1. Schematic diagram of preparation and morphological characteristics of GQDs, GQDs/BWO, and GQDs/BWO$_{6-x}$. (a) schematic diagram of the GQDs/BWO$_{6-x}$ preparation process. (b) SEM of GQDs/BWO. (c) SEM of GQDs/BWO$_{6-x}$. (d) TEM of GQDs. inset: the size distribution of the prepared GQDs. (e) TEM of GQDs/BWO. (f) TEM of GQDs/ BWO$_{6-x}$. (g) enlarged TEM of GQDs/BWO$_{6-x}$. (h) DF-STEM image of GQDs/BWO$_{6-x}$. (i)-(l) elemental mapping images of the region indicated in Fig. 1h. (m) intensity profiles along the two green lines of Fig. 1g.

photocatalyst were suspended into a glass reactor containing a mixture of 90 mL of DI water and 10 mL triethanolamine (TEA, a sacrificial agent). Temperature of the reactor was controlled at 0 °C by a circulating water-cooling system. Before illumination, the reaction system was first vacuated and then slowly pumped with high purity CO_2 (99.99%) until the pressure became steady at 0 MPa. The above operation was repeated three times to exhaust air from the reaction system thoroughly. After stirring for 30 min, the adsorption-desorption balance between the photocatalyst and CO_2 could be established, and the Xe lamp was then turned on to start the photocatalytic experiment. Gas-phase products were sampled from the glass chamber at given time intervals (1 h) for quantitative analyses of CO and other carbon-based products by an on-line gas chromatograph (GC-7806).

Isotope labeling experiments were carried out according to the procedures used by Wang et al. [21]. Typically, $^{13}CO_2$ gas (Isotope purity, 99% and chemical purity, 99.9%, Tokyo Gas Chemicals Co., Ltd.) was employed instead of pure $^{12}CO_2$ gas as the carbon source with the same reaction setting as described above. Gas products were analyzed by gas chromatography-mass spectrometry (JMS-K9, JEOL-GCQMS, Japan, and 6890N Network GC system, Agilent Technologies, USA) for detecting the products of ^{13}CO and other gas products.

2.4. Computational methods

Density functional theory (DFT) calculations were conducted using *Materials Studio* software [22]. Based on XRD results, the preferentially exposed facet of Bi_2WO_6 was (113). The (113) facet, with a thickness of four atomic layers, was therefore chosen as a basic configuration to build the top surface of Bi_2WO_6 with GQDs and oxygen vacancy. The height of the vacuum layer is set as 14 Å to avoid the interaction of neighboring layers.

The Perdew–Burke–Ernzerhof (PBE) of the generalized gradient approximation [23] was used as the exchange-correlation function. A plane wave cut-off energy of 550 eV, a $3 \times 3 \times 1$ k-point mesh for the Brillouin zone sampling, and the ultrasoft pseudopotential were set for the accurate geometry optimizations and electronic structure calculations. The DFT+U approach was introduced to accurately describe our systems with localized d electrons (i.e., W 5d in the Bi_2WO_6). The +U parameter was set to 3.0 eV for W 5d orbitals. The convergence tolerance of energy, maximum force, and maximum displacement were set to 1.0×10^{-5} eV/atom, 0.03 eV/Å, and 0.001 Å, respectively.

Oxygen vacancies in the BWO_{6-x} could be classified into two types: those Vo originated from cleavage of the Bi-O bond and those from the W-O bond (ESI†, Table S1). To choose a more stable Vo type and thus simplify the configuration of BWO_{6-x} and $GQDs/BWO_{6-x}$, the corresponding formation energies were calculated, which is given by Eq. (1),

$$E_F = E_{BWO6-x} - E_{BWO} - E_O \qquad (1)$$

where ΔE_{B1} is the formation energy of oxygen vacancy. E_{BWO}, E_{BWO6-x}, and E_O are the energies of perfect BWO semiconductor, BWO_{6-x} with one type of oxygen vacancies, and one single oxygen atom, respectively. The energy of one single oxygen atom is half of the total energy of an O_2 molecule ($1/2E_{O2}$). The calculation results were listed in Table S1, indicating that type 1 (Vo from W-O) is more stable with a higher E_F absolute value (-25.42 eV) compared to type 2 (-24.46 eV) and thus employed as the foundation for constructing the $GQDs/BWO_{6-x}$ model.

Similarly, possible adsorption sites of CO_2 on the $GQDs/BWO_{6-x}$ surface were constructed, and their most stable configurations were determined according to the binding energy maximum principle (Table S1). The final configuration for CO_2 adsorption sites can be seen in Section 3.4.

3. Results and discussion

3.1. Physicochemical characteristics

The SEM and TEM images of GQDs, GQDs/BWO, and $GQDs/BWO_{6-x}$ are shown in Fig. 1. The flower-like $GQDs/BWO_{6-x}$ microspheres were assembled from nanosheets. Fig. 1c shows that the average size of prepared GQDs was 2.2 nm. The lattice fringes, 0.313 nm, correspond to the (113) facet of Bi_2WO_6, which is one of the main exposed facets. The disordered lattice fringe of the boundary layer (surrounded by the blue dotted line) should be attributed to the existence of Vo. As shown in Fig. 1 m, the intensity profiles in the BWO (113) lattice region are uniformly distributed along the indicated green line l. In comparison, the intensity profiles in the boundary region are irregularly distributed along green line 2, suggesting the possible existence of Vo in the boundary region. The disorder in the boundary region presumably arises from alkali etching which partially dissolved the Bi_2WO_6 crystal, thus introducing the oxygen vacancy. It can be seen from the elemental mapping images (Fig. 1h-l) that, in addition to the uniform distributions of B, W, and O from BWO, a small amount of C originated from GQDs was homogeneously dispersed on the $GQDs/BWO_{6-x}$ sample.

Fig. 2a shows the XRD pattern of BWO, GQDs/BWO, BWO_{6-x}, and $GQDs/BWO_{6-x}$. The peaks at 28.4°, 32.9°, 47.2°, 56.1°, and 58.4° were indexed to the (113), (200), (220), (313), and (119) facets of orthorhombic Bi_2WO_6 (JCPDS no. 73–2020), respectively. No peaks corresponding to GQDs were observed, which may be due to the tiny size and small amount of GQDs and high dispersion on the Bi_2WO_6 surface. As seen in Fig. 2b, the (020)/(200) peaks of GQDs/BWO, BWO_{6-x}, and $GQDs/BWO_{6-x}$ increasingly showed a shift towards a higher 2theta angle compared to BWO, with $GQDs/BWO_{6-x}$ exhibiting an upmost and most apparent shift. The upshifts may be caused by residual surface stress of Bi_2WO_6 arising from oxygen vacancy [22] and GQDs.

To confirm the successful introduction of GQDs onto the BWO surface, FT-IR spectra of GQDs/BWO and $GQDs/BWO_{6-x}$ were recorded. Fig. 2c shows the peaks at 1065 cm^{-1} assigned to the vibration of the C-O bond of GQDs. These peaks were absent in the spectrum of pure Bi_2WO_6.

Peaks at 576, 728, and 1389 cm^{-1} were assigned to the stretching vibration of W-O, Bi-O, and to the W-O-W bridging stretching, respectively. The intensities of these absorptions were seen to increase with the introduction of Vo (BWO_{6-x}, $GQDs/BWO_{6-x}$). The data indicate that more Bi-O and W-O bonds were exposed after alkali etching.

XPS analysis was performed further to confirm the existence of Vo on $GQDs/BWO_{6-x}$. The C1s peak region can be deconvoluted into three peaks (Fig. 2e). The central C 1s peak at ~284.8 eV may arise from the lattice structure of sp2 hybridized carbon atoms in the GQDs structure [18]. The flat peaks at 287.0 eV correspond to the few C–O bonds contained in the GQDs. The asymmetric O 1s peak of BWO (Fig. 2f) could be deconvoluted into three peaks, ascribing to the lattice oxygen atoms as forms of Bi-O and W-O, and the surface-adsorbed oxygen species (hydroxyl, H_2O, etc.), respectively [24]. Surface oxygen vacancies tend to adsorb more surface oxygen species, which would increase the peak area at ~530 eV. This would explain the peak area increase at 530.3 eV for $GQDs/BWO_{6-x}$ compared to GQDs/BWO. In addition, O 1s binding energy (530.3 eV) of $GQDs/BWO_{6-x}$ showed a downward shift of 0.6 eV compared to $GQDs/BWO_6$ (530.9 eV). The shift can be ascribed to the change of electron density around O atoms after Vo introduction [19, 25].

### 3.2. UV–vis and photoelectrochemical properties

The UV–vis absorption properties of BWO, BWO_{6-x}, GQDs/BWO, and $GQDs/BWO_{6-x}$ were studied by UV–vis diffuse reflectance spectrometry. Fig. 3a shows that $GQDs/BWO_{6-x}$ exhibited much stronger absorption in the UV region and the visible light range than the other catalysts.

The TR-PL decay curves of BWO and $GQDs/BWO_{6-x}$ were recorded in
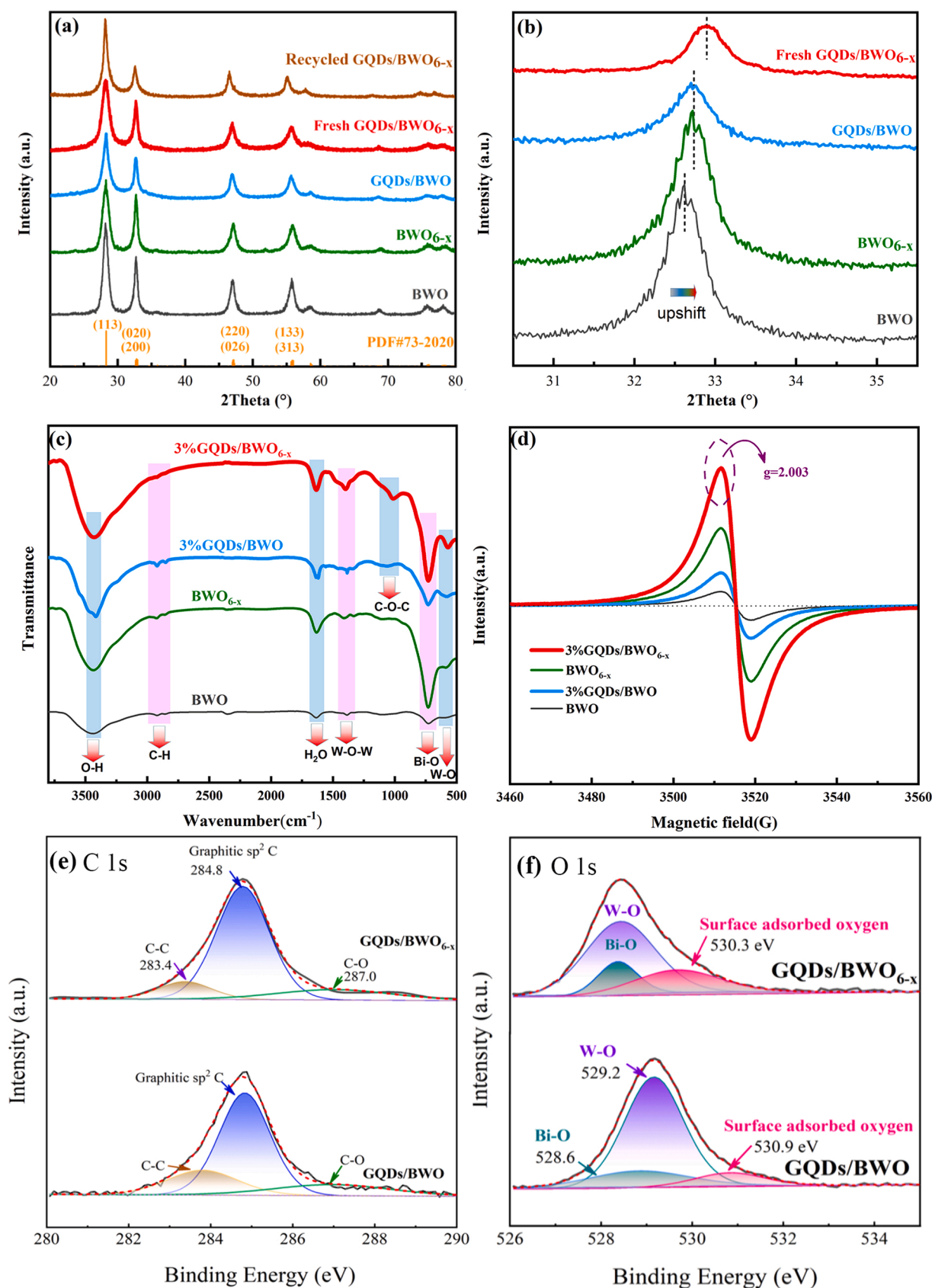
Fig. 2. XRD and spectroscopic characteristics of BWO, BWO_{6-x}, GQDs/BWO, and GQDs/BWO_{6-x}. (a) XRD spectra. (b) enlarged regions of XRD. (c) IR spectra. (d) EPR. (e) C 1s peak region of XPS and (f) O 1s peak region.
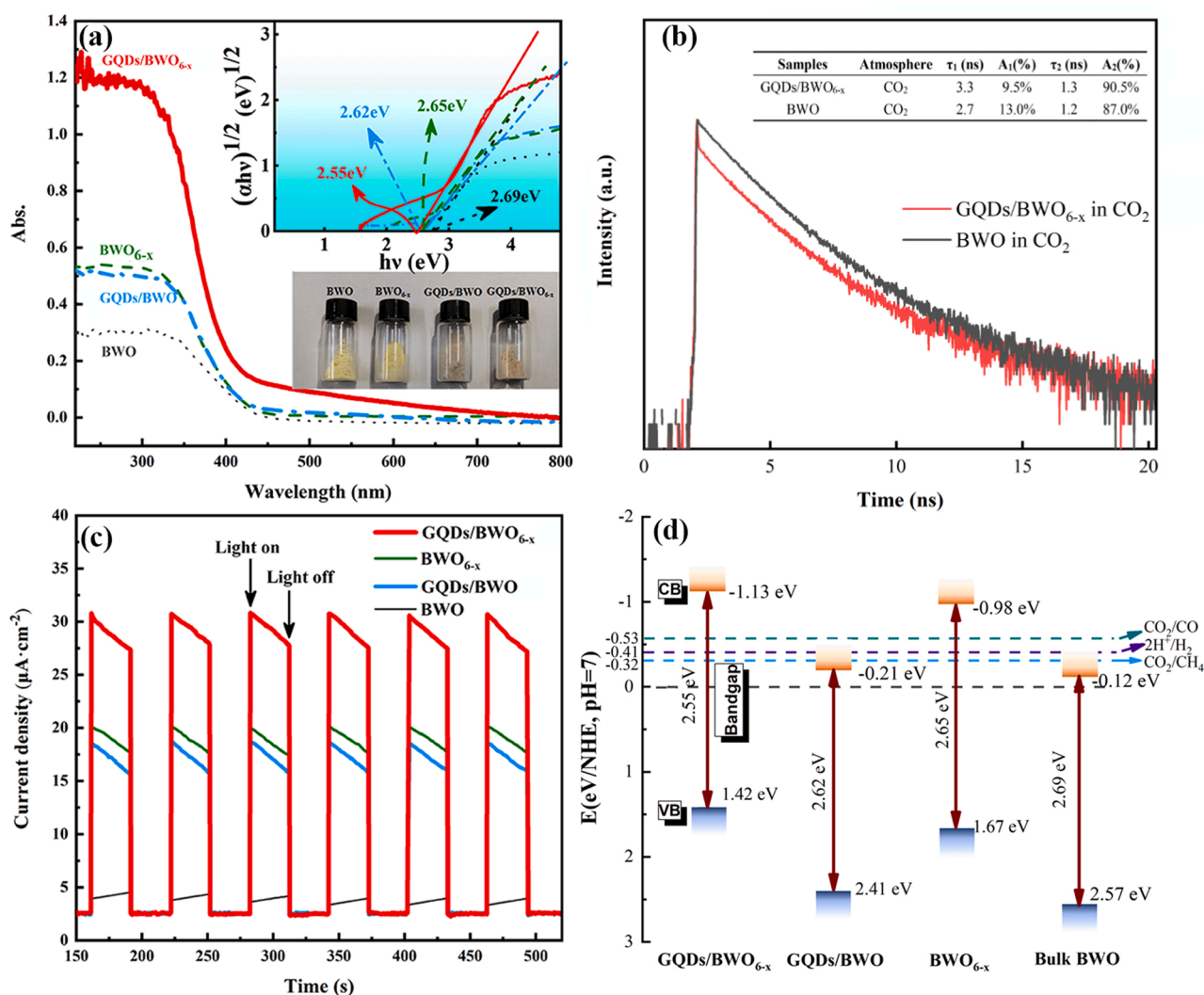
Fig. 3. Band structure and photoelectric properties of BWO, GQDs/BWO, BWO$_{6-x}$, and GQDs/BWO$_{6-x}$. (a) UV–vis diffuse reflectance spectra and bandgaps (inset). (b) Time-resolved photoluminescence decay spectra of BWO and GQDs/BWO$_{6-x}$. (c) The *i*-*t* curves. (d) Band structures.

Fig. 3b. The inset shows the calculated photoluminescence decay lifetime (τ_1 and τ_2) and their magnitude factors (A$_1$ and A$_2$) of charge carriers. The GQDs/BWO$_{6-x}$ composite had both longer fast decay lifetime (τ_1 =3.3 ns) and slow decay lifetime (τ_2 =1.3 ns) in CO$_2$ than that of BWO (τ_1 =2.7 ns, τ_2 =1.2 ns), indicating its better separation efficiency of photogenerated charge carriers [21].

The *i*–t, PL spectra, and EIS curves were measured to investigate further the role of GQDs and Vo in suppressing the recombination of photogenerated h$^+$/e$^-$ pairs. The *i*–t curves are shown in Fig. 3c. The photocurrent intensities of GQDs/BWO$_{6-x}$, BWO$_{6-x}$, and GQDs/BWO are 13, 8.2, and 7.5 times higher than pristine BWO, respectively. The weak intensity of photoluminescence is an indication of the low recombination rate of light-driven h$^+$/e$^-$ pairs (ESI†, Fig. S2a) [26]. Photoluminescence intensity of the catalysts followed the order of GQDs/BWO$_{6-x}$ < BWO$_{6-x}$ < GQDs/BWO < BWO. Fig. S2b exhibits that the SPS of GQDs/BWO$_{6-x}$ reaches the highest intensity. All the above results indicated the highest capability of GQDs/BWO$_{6-x}$ to suppress the recombination of h$^+$/e$^-$ pairs. The EIS spectra were measured to reveal the charge transfer resistance at the solid/solution interface. Fig. S2c exhibits that the semicircle diameter of GQDs/BWO$_{6-x}$ is the least among all the samples, meaning a fast charge transfer process.

Fig. 3d shows all the Eg values identified by the Tauc plot method [7]. Eg of pristine Bi$_2$WO$_6$, BWO$_{6-x}$, GQDs/BWO, and GQDs/BWO$_{6-x}$ were determined to be 2.69, 2.65, 2.62, and 2.55 eV, respectively. The

lower bandgap of GQDs/BWO$_{6-x}$ was beneficial to enhance visible-light absorption.

XPS valence band spectra (Fig. S1) were recorded to determine the valence band (VB) edge of the above samples. The VB edge of BWO, BWO$_{6-x}$, GQDs/BWO, and GQDs/BWO$_{6-x}$ were identified as 2.57, 1.67, 2.41, and 1.42 eV, respectively. According to the XPS valence spectra results and the Eg values, the detailed band structures of the above samples can be obtained and shown in Fig. 3d. The conduction bond (CB) edge of BWO moved to lower potentials, i.e., − 0.95 eV of BWO$_{6-x}$ and − 1.13 eV of GQDs/BWO$_{6-x}$, which was mainly attributed to Vo decoration on its surface. This result indicated that the photogenerated CB electrons of GQDs/BWO$_{6-x}$ owned a stronger reduction power than GQDs/BWO for converting CO$_2$ to CO and CH$_4$, and GQDs/BWO$_{6-x}$ possessed a narrower bandgap for enhancing solar light utilization efficiency.

3.3. Control experiments and activity test

Four control experiments were conducted to investigate the origin of the carbonaceous gas products. The result (Table S2) shows that neither CH$_4$ nor CO was detected in the cases of light off, no entry of CO$_2$, or no TEA, indicating that the light irradiation, CO$_2$, and TEA were indispensable for the photocatalytic formation of carbonaceous fuels. However, when GQDs/BWO$_{6-x}$ was absent, a tiny amount of CO

(2.7 μmol·g^{-1}·h^{-1}) and H$_2$ (4.2 μmol·g^{-1}·h^{-1}) under 3 h of light irradiation was detected. The above results ascertain that neither the photocatalysts nor TEA were a potential source of CO. The carbonaceous products under visible light irradiation were derived from the photoreduction of CO$_2$. By the way, all the CO and H$_2$ yield data in this paper were obtained by deducting the corresponding CO and H$_2$ yields, which were measured in the case of no addition of photocatalyst under various irradiation times to expel the calculation error and precisely evaluate the CO yield.

We employed the isotope-labeled carbon dioxide (^{13}CO$_2$) as a substitute gas to further determine the origin of CO. As shown in the inset of Fig. 4c, the total ion chromatographic peak at 7.66 min can be assigned to CO. The primary MS signal at $m/z = 29$ with a high abundance (Fig. 4c) belonged to ^{13}CO, and the others (^{13}C at $m/z = 13$ and O at $m/z = 16$) corresponded to the fragments of ^{13}CO, confirming that the CO product exactly originated from the CO$_2$ photoreduction over GQDs/BWO$_{6-x}$. In addition, the inevitable intake of air into the GC sampling needle during the sampling course would lead to the appearance of obvious peaks of O$_2$ (3.63 min) and N$_2$ (4.23 min) in the total ion chromatography.

As illustrated in Fig. 4a, the maximum CO yield per hour for GQDs/BWO$_{6-x}$ was 43.9 μmol·g^{-1}·h^{-1} under visible light irradiation over 5 h. In comparison, the maximum CO yield for GQDs/BWO was 30.1 μmol·g^{-1}·h^{-1}, and the maximum CO yield for BWO was

26.6 μmol·g^{-1}·h^{-1} under the same conditions. The CO yield of GQDs/BWO$_{6-x}$ was ab.1.7 times BWO.

The stability of GQDs/BWO$_{6-x}$ was further investigated by a four-run recycling experiment under the same condition. The 5 h cumulative yield falls by 21% for CO after four cycles (Fig. 4b), indicating that GQDs/BWO$_{6-x}$ possesses good cyclic stability. In addition, the XRD characteristic peaks of the recycled sample indexed to the (113), (020), (220), and (133) facets (Fig. 2a) kept almost unchanged as compared to the fresh sample, showing the stability of GQDs/BWO$_{6-x}$ intuitively.

3.4. Insights into the mechanism for the enhanced photocatalytic activity

The in-situ CO$_2$ adsorption DRIFTS IR spectra under visible light irradiation were recorded on GQDs/BWO$_{6-x}$ samples to unravel the reaction pathway and elucidate the underlying reasons for the enhanced photocatalytic activity. As shown in Fig. 5a, no intermediate peak was observed when CO$_2$ initially dissolves in the TEA aqueous solution (Dark for 0 min). After 30 min in the dark or 20–60 min light irradiation, the dissolved CO$_2$ started to form monodentate carbonate (ν_s(CO$_3$) mode of m-CO$_3$$^{2-}$, 1476 cm^{-1}), bidentate carbonate (ν_s(CO$_3$) modes of b-CO$_3$$^{2-}$, 1290 cm^{-1}), chelating-bridged carbonate (c-CO$_3$$^{2-}$, 1294 cm^{-1}), bicarbonate (δ(OH) modes of HCO$_3$$^-$, 1208 cm^{-1}), the active intermediate *CO$_2$ (*CO$_2$ denotes the CO$_2$ molecule adsorbed at the active site. 1652 cm^{-1}, 1290 cm^{-1}), and *CHO (1096 cm^{-1}) [27,28]. It is worthy to
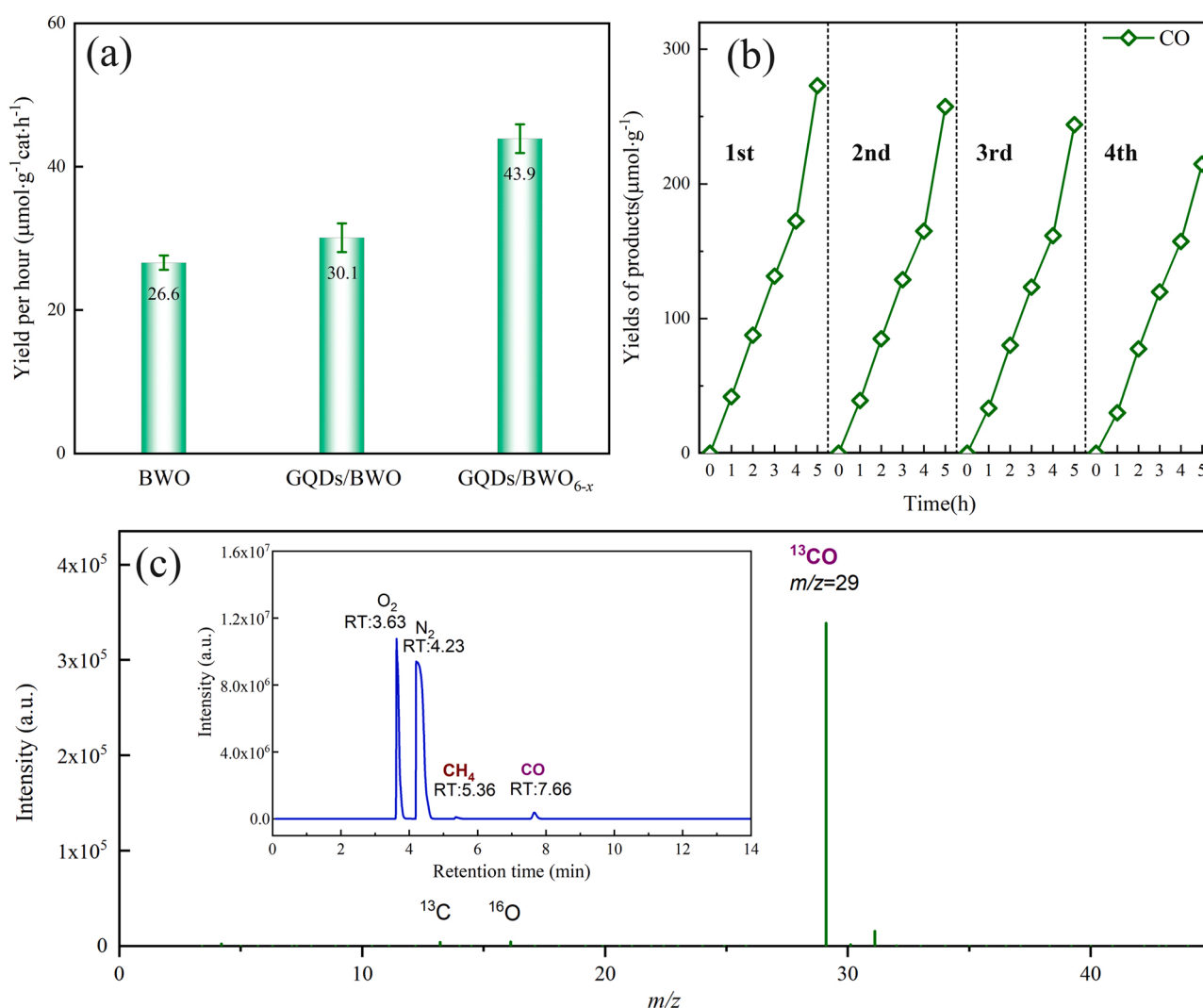
Fig. 4. (a) CO yield per hour of BWO, GQDs/BWO, and GQDs/BWO$_{6-x}$. (b) Stability test of GQDs/BWO$_{6-x}$ using four-run recycling experiments under visible light irradiation at 0 °C. (c) Mass spectra of ^{13}CO and total ion chromatography (inset) over GQDs/BWO$_{6-x}$ in the photocatalytic reduction of ^{13}CO$_2$.
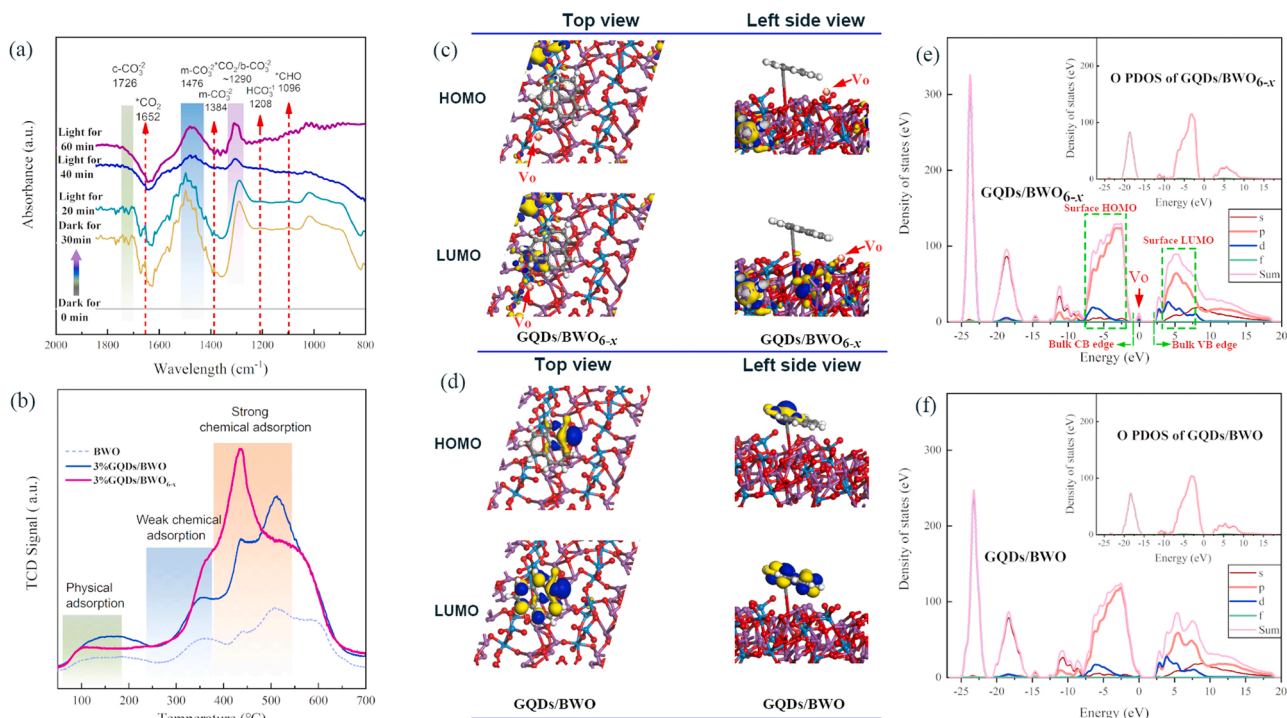
Fig. 5. (a) The in-situ DRIFTS IR spectra of humid CO_2 over GQDs/BWO$_{6-x}$. (b) CO_2-TPD profiles of BWO, GQDs/BWO, and GQDs/BWO$_{6-x}$. HOMO and LUMO of (c) GQDs/BWO$_{6-x}$ and (d) GQDs/BWO. PDOS of (e) GQDs/BWO$_{6-x}$, and (f) GQDs/BWO. Note: the colored balls represent different atoms: red, oxygen (O); gray, carbon (C); white, hydrogen (H); purple, bismuth (Bi); blue, tungsten (W).

note that the adsorption peaks at $1620 - 1689$ cm^{-1} and 1290 cm^{-1} are assigned to the characteristic vibration mode of *CO_2, and the appearance of *CO_2 peak implies the successful activation of the adsorbed CO_2 on the surface of GQDs/BWO$_{6-x}$ [29].

The temperature-programmed desorption (TPD-CO_2) was performed to understand the interactions between the composite surfaces and CO_2. As shown in Fig. 5b, the peak intensity of GQDs/BWO$_{6-x}$ is above that of pure GQDs/BWO, indicating higher CO_2 adsorption capacities than GQDs/BWO, which would benefit the photocatalytic conversion of CO_2. Similarly, BWO$_{6-x}$ possessed more robust adsorption capacities than BWO. The peaks in the temperature ranges of 50 ℃− 180 ℃, 180 ℃− 360 ℃ and 360 ℃− 520 ℃, corresponded to strong physical adsorption, weak and powerful chemical adsorption toward CO_2, respectively. For the type of powerful chemical adsorption, the peak intensity and area of GQDs/BWO$_{6-x}$ at $360 - 520$ ℃ were 20 and 5.2 times higher than those of BWO and GQDs/BWO, respectively. It confirmed the existence of the chemical binding of CO_2 molecules with the GQDs/BWO$_{6-x}$ surface atoms.

The in-situ EPR (Fig. S3) was performed to identify the free radical type over GQDs/BWO$_{6-x}$ during the photocatalytic CO_2 reduction. It displays a clear DMPO- ·O_2^- signal but an extremely weak DMPO-•OH signal. An increment in the DMPO- ·O_2^- signal as a function of irradiation time confirmed the correlation of ·O_2^- generation with photocatalysis. The weak intensity of the DMPO- •OH signal could be caused by the scavenging effect of TEA toward the •OH free radical.

The effect of GQDs and oxygen vacancy on the band structures of composites were further unraveled by calculating the HOMO-LUMO and DOS of composites. As is known, the electrons of HOMO are most weakly held and tend to flow from HOMO on one molecule to LUMO on the other molecule. Fig. 5b shows that both HOMO and LUMO of GQDs/BWO mainly confine in the GQDs molecules, indicating the photogenerated electrons are hard to separate and lead to a high recombination rate with photogenerated holes. In comparison, the photogenerated electrons on the Bi and O atoms that are remote to Vo tend to flow to the Vo-neighboring W and O atoms. It means that the

photogenerated electrons are easy to separate with holes.

The calculation results of the partial density of states (PDOS) of GQDs/BWO$_{6-x}$ and GQDs/BWO indicated that the surface HOMO and LUMO of both samples were mainly composed of O 2p electrons. The CB edge of GQDs/BWO$_{6-x}$ became more negative than that of GQDs/BWO, consistent with the measured values given by Fig. 3d, and manifested an enhanced reduction ability. Meanwhile, as shown in Fig. 5d, a new band marked with a red arrow appeared in the forbidden band of GQDs/ BWO$_{6-x}$, but no intermediate band emerged for GQDs/BWO. This new band should belong to Vo, leading to a bandgap narrowing and accepting more excited electrons.

Charge density differences (Fig.S4) showed that the electron clouds were mainly distributed over the H atoms of GQDs and O atoms of BWO. The distributions of electronic accumulation in GQDs showed a clear tendency of electrons to move toward oxygen vacancy. Combined with the HOMO and LUMO results, we speculated that GQDs could acted as photosensitizers to generate a few electrons, which would transfer to the Vo-neighboring sites. Meanwhile, a mass of photogenerated electrons moved from the Vo-remote atoms of BWO to the Vo-neighboring sites to reduce the adsorbed CO_2 molecules.

In terms of investigating the photocatalytic reduction route, the following equations can express the main steps according to the reference [30].

$$GQDs/BWO_{6-x} + h\nu \rightarrow h^+ + e^- \tag{2}$$

$$CO_2 \rightarrow *CO_2 \tag{3}$$

$$*CO_2 + 2 H^+ + 2e^- \rightarrow CO + H_2O \tag{4}$$

$$*CO_2 + 8 H^+ + 8e^- \rightarrow CH_4 + 2 H_2O \tag{5}$$

Regarding Eq.2, various adsorption configurations for *CO_2 were constructed (Table.S3), attempting to identify an optimal adsorption site by comparing the adsorption energy. The CO_2 molecule tended to bond weakly with the catalyst surface through a single-site bonding between the 2p orbital of sole C or O atom of the CO_2 molecule and the orbital of

non-metal atoms (such as the sole C of CO_2 with O: C_{2p}-O_{2p}) or metal atoms of the photocatalyst surface (such as the sole O of CO_2 with Bi: O_{2p}-W_{5d}) [31]. Besides, according to the impressive CO_2 reduction routes proposed by Sheng et al. [29], the single-site bonding readily formed the m-CO_3^{2-} intermediate while the dual-site bonding (i.e., 2p orbitals of both C and O atoms of CO_2 had a bonding interaction with two close metal or non-metal atoms on the photocatalyst surface) readily form the b-CO_3^{2-}. As seen in Fig. 5a, the signals of m-CO_3^{2-} on the surface of GQDs/BWO$_{6-x}$ are more intensive than that of b-CO_3^{2-}. It suggested that the single-site bonding of C-O rather than dual-sites bonding was the priority selection for the CO_2 adsorption configuration in this case, although the dual-sites bond could be more robust. Based on the above discussion and for simplification of DFT calculation, two single-site bonding configurations were constructed. One was the P1 configuration, where CO_2 was adsorbed on the surface by bonding its sole C with the Vo-neighboring O atom. Another was the P2 configuration, where its C bonded with an O atom far away Vo. The calculation result indicated that P1 (−16.46 eV) was more stable than P2 (−13.36 eV), and the CO_2 molecules were more easily absorbed at the surface Vo sites.

DFT calculation results of molecular bonding energy on the photocatalyst surface were further used to roughly observe the trend of adsorption energy for intermediates and illustrate the CO_2 activation mechanism. Fig. 6a and b display the bonding energy profiles and the corresponding intermediate configurations. The adsorbed CO_2 molecules on Bi_2WO_6 and GQDs/BWO$_{6-x}$ were initially hydrogenated to *COOH and then converted to *CO and *OH, which further transformed to *CO and H_2O, respectively [32]. The intermediate *CO that bonded at the Vo-neighboring sites could be desorbed from the GQDs/BWO$_{6-x}$ surface to generate CO (pathway (1)) or hydrogenated to form *CHO (pathway (2)). The CO desorption energy for GQDs/BWO$_{6-x}$ was identified to be − 0.71 eV, close to that for Bi_2WO_6 (−0.59 eV). This result implied that the surfaces of GQDs/BWO$_{6-x}$ and BWO had a similar capability for desorption of *CO to form free CO. Meanwhile, GQDs/BWO$_{6-x}$ had lower *CHO generation energy (absolute value: 0.70 eV) than bulk BWO (absolute value: 1.30 eV), indicating that the intermediate *CO for GQDs/BWO$_{6-x}$ was easier to be protonated to form

CH$_4$. More importantly, according to Li et al. [32], the protonation of *COOH to form *CO was a rate-determining step. The relative energy barrier for the transformation of *COOH-GQDs/BWO$_{6-x}$ to *CO-GQDs/BWO$_{6-x}$ (−0.46 eV - (−0.62 eV) = 0.16 eV) was lower than that for *COOH-BWO to *CO-BWO (−0.2 eV - (−1.32 eV) = 1.12 eV), meaning that the decoration by GQDs and Vo were beneficial to accelerate the transformation of *COOH to *CO. The above analysis is consistent with the results of activity tests.

Based on the above results, a possible mechanism of photocatalytic reduction of CO_2 can be speculated (Fig. 6c and d). BWO was responsible for generating a mass of electrons under light irradiation, and GQDs could also produce a few electrons. Most photogenerated electrons preferred to move to the Vo-neighboring atoms, accelerating the charge separation. GQDs enabled the CB of BWO to be more negative and intensified the visible light response capacity. More negative CB was beneficial to enhance the reduction capability of composites. Oxygen vacancies served as the adsorption and activation sites for CO_2. The CO_2 molecule was readily adsorbed at the Vo sites to form *CO_2 and then converted to *CO_2- by gaining the photogenerated electrons. Other intermediates, including *CHO and *COOH, were further formed by combing with H^+ formed by dissociation of H_2O under the attack of holes and·O_2^- free radicals. Finally, CO, CH$_4$, and other carbonaceous fuels were produced.

4. Conclusions

GQDs modified BWO$_{6-x}$ was successfully prepared by a microwave-assisted hydrothermal process. The as-developed GQDs/BWO$_{6-x}$ nanocomposites demonstrated impressive visible light photoactivity for CO_2 reduction to CO. The activity test results showed that the maximum CO yield per hour for GQDs/BWO$_{6-x}$ was 43.9 µmol·g^{-1}·h^{-1} under visible light irradiation over three hours. The CO yield of GQDs/Bi_2WO_{6-x} is 1.7-fold higher than pristine BWO. The isotope-labeled experiment showed that the prominent peak at $m/z = 29$ achieved a high abundance of $^{13}CO_2$, proving that CO indeed originated from the photocatalytic reduction of CO_2.
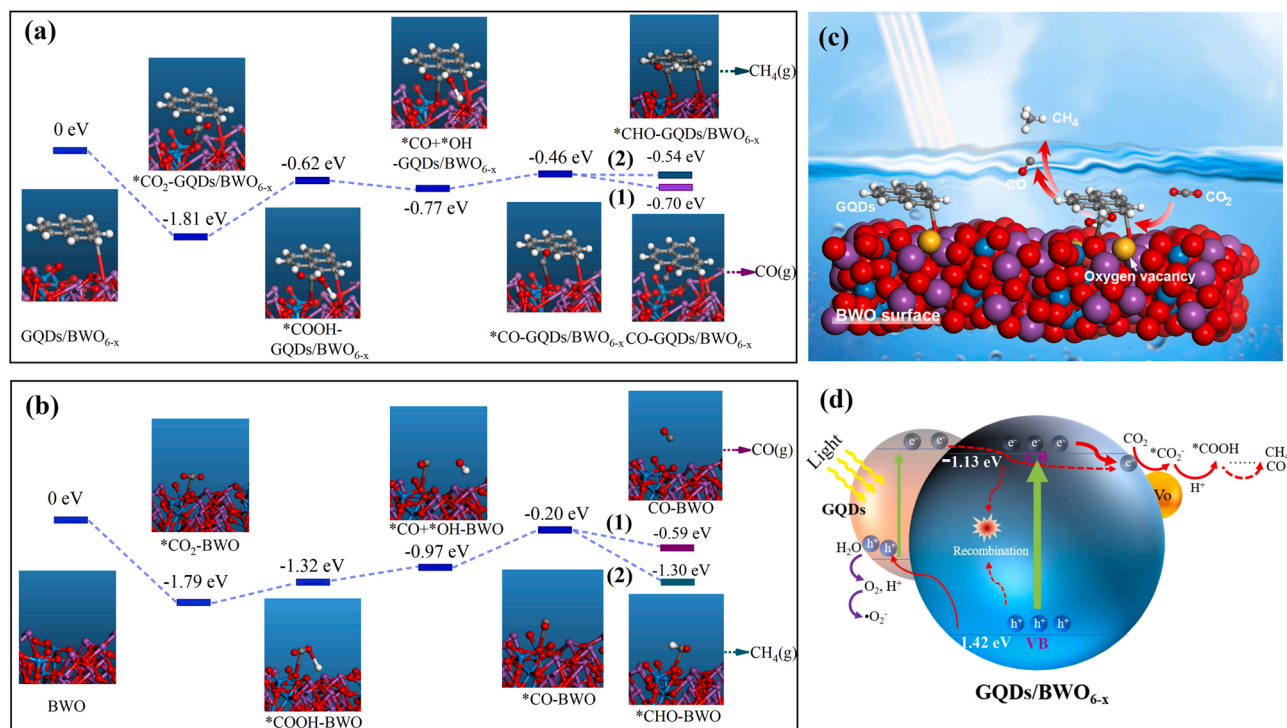
Fig. 6. Free energy diagrams for the reduction of CO_2 to CO or *CHO over (a) GQDs/BWO$_{6-x}$ and (b) BWO. (c) Illustration of GQDs/BWO$_{6-x}$ surface microstructure. (d) Illustration of a possible mechanism for photocatalytic CO_2 reduction by GQDs/BWO$_{6-x}$.

The DFT calculation results revealed that the energy barrier of GQDs/BWO$_{6-x}$ (0.16 eV) for transforming the intermediate *COOH to *CO, a rate-determining step, was lower than BWO (1.12 eV), leading to its enhanced photocatalytic performance. Oxygen vacancies localized the photogenerated electrons and promoted the electron-hole separation efficiency. The UV–vis diffuse reflectance spectra indicated that GQDs intensified the visible-light absorption capability. Besides, the modification of GQDs and Vo enabled the CB of BWO (−0.12 eV) to be more negative (CB of GQDs/Bi$_2$WO$_{6-x}$: −1.13 eV), which is beneficial in enhancing the reduction capability of composites.

CRediT authorship contribution statement

Shaofeng Xiong: Conceptualization, DFT calculation, Writing – original draft, Supervision. **Shundong Bao:** Characterization, Formal analysis. **Weian Wang:** Photocatalyst preparation, Characterization. **Jian Hao**: Investigation, Validation. **Yu Mao:** Suggestion on the DFT calculation. **Pingle Liu:** Writing – review & editing. **Yanping Huang:** Suggestion on the DFT calculation. **Zhengkang Duan:** Formal analysis. **Yang Lv:** Formal analysis. **Donghong Ouyang:** Formal analysis.

Declaration of Competing Interest

The authors declare that they have no known competing financial interests or personal relationships that could have appeared to influence the work reported in this paper.

Acknowledgements

Appendix A. Supporting information

Supplementary data associated with this article can be found in the online version at doi:10.1016/j.apcatb.2021.121026.

References

[1] C. Li, J. Ciston, M.W. Kanan, Electroreduction of carbon monoxide to liquid fuel on oxide-derived nanocrystalline copper, Nature 508 (2014) 504–508, https://doi.org/10.1038/nature13249.

[2] T. Inoue, A. Fujishima, S. Konishi, K. Honda, Photoelectrocatalytic reduction of carbon dioxide in aqueous suspensions of semiconductor powders, Nature 277 (1979) 637–638, https://doi.org/10.1038/277637a0.

[3] Y. Yuan, L. Ruan, J. Barber, S. Joachim, C. Xue, Hetero-nanostructured suspended photocatalysts for solar-to-fuel conversion, Energy Environ. Sci. 7 (2014) 3934–3951. ⟨https://pubs_rsc.gg363.site/en/content/articlelanding/2014/ee/c4ee02914c/unauth⟩.

[4] C. Zhang, Y. Zhu, Synthesis of square Bi$_2$WO$_6$ nanoplates as high-activity visible-light-driven photocatalysts, Chem. Mater. 17 (2005) 3537–3545, https://doi.org/10.1021/cm0501517.

[5] H. Gu, G. Xing, H. Gu, Z. Chai, X. Wang, A novel strategy to promote photo-oxidative and reductive abilities via the construction of a bipolar Bi$_2$WO$_6$/N-SrTiO$_3$ material, RSC Adv. 7 (2017) 52218–52226, https://doi.org/10.1039/C7RA10932F.

[6] Y. Zhou, Z. Tian, Z. Zhao, Q. Liu, J. Kou, X. Chen, J. Gao, S. Yan, Z. Zou, High-yield synthesis of ultrathin and uniform Bi$_2$WO$_6$ square nanoplates benefitting from photocatalytic reduction of CO$_2$ into renewable hydrocarbon fuel under visible light, ACS Appl. Mater. Interfaces 3 (2011) 3594–3601, https://doi.org/10.1021/am2008147.

[7] X. Zhang, G. Ren, C. Zhang, R. Li, Q. Zhao, C. Fan, Photocatalytic reduction of CO$_2$ to CO over 3D Bi$_2$MoO$_6$ microspheres: simple synthesis, high efficiency and selectivity, reaction mechanism, Catal. Lett. 150 (2020) 2510–2516, https://doi.org/10.1007/s10562-020-03182-3.

[8] L. Yuan, K. Lu, F. Zhang, X. Fu, Y. Xu, Unveiling the interplay between light-driven CO$_2$ photocatalytic reduction and carbonaceous residues decomposition: a case study of Bi$_2$WO$_6$-TiO$_2$ binanosheets, Appl. Catal. B 237 (2018) 424–431, https://doi.org/10.1016/j.apcatb.2018.06.019.

[9] W. Jo, S. Kumar, S. Eslava, S. Tonda, Construction of Bi$_2$WO$_6$/RGO/g-C$_3$N$_4$ 2D/2D/2D hybrid Z-scheme heterojunctions with large interfacial contact area for efficient charge separation and high-performance photoreduction of CO$_2$ and H$_2$O into solar fuels, Appl. Catal. B 239 (2018) 586–598, https://doi.org/10.1016/j.apcatb.2018.08.056.

[10] X. Kong, W. Tan, B. Ng, S. Chai, A. Mohamed, Harnessing vis–NIR broad spectrum for photocatalytic CO$_2$ reduction over carbon quantum dots-decorated ultrathin Bi$_2$WO$_6$ nanosheets, Nano Res. 10 (2017) 1720–1731, https://doi.org/10.1007/s12274-017-1435-4.

[11] L. Zhang, W. Wang, H. Wang, X. Ma, Z. Bian, Design of inorganic–organic hybrid photocatalytic systems for enhanced CO$_2$ reduction under visible light, Chem. Eng. Sci. 207 (2019) 1246–1255, https://doi.org/10.1016/j.ces.2019.07.049.

[12] W. Zhang, J. Xue, Q. Shen, S. Jia, J. Gao, X. Liu, H. Jia, J. Alloy. Compd. 870 (2021), 159400, https://doi.org/10.1016/j.jallcom.2021.159400.

[13] J. Li, M. Zhang, Z. Guan, Q. Li, C. He, J. Yang, Synergistic effect of surface and bulk single-electron-trapped oxygen vacancy of TiO$_2$ in the photocatalytic reduction of CO$_2$, Appl. Catal. B 206 (2017) 300–307, https://doi.org/10.1016/j.apcatb.2017.01.025.

[14] M. Liang, T. Borjigin, Y. Zhang, B. Liu, H. Liu, H. Guo, Controlled assemble of hollow heterostructured g-C$_3$N$_4$@CeO$_2$ with rich oxygen vacancies for enhanced photocatalytic CO$_2$ reduction, Appl. Catal. B 243 (2019) 566–575, https://doi.org/10.1016/j.apcatb.2018.11.010.

[15] Z. Zhang, W. Wang, E. Gao, M. Shang, J. Xu, Enhanced photocatalytic activity of Bi$_2$WO$_6$ with oxygen vacancies by zirconium doping, J. Hazard. Mater. 196 (2011) 255–262, https://doi.org/10.1016/j.jhazmat.2011.09.017.

[16] C. Guo, Y. Dong, H. Yang, C. Li, Graphene quantum dots as a green sensitizer to functionalize ZnO nanowire arrays on F-doped SnO$_2$ glass for enhanced photoelectrochemical water splitting, Adv. Energy Mater. 3 (2013) 997–1003, https://doi.org/10.1002/aenm.201300171.

[17] C. Bao, L. Song, W. Xing, B. Yuan, C.A. Wilkie, J. Huang, Y. Guo, Y.J. Hu, Preparation of graphene by pressurized oxidation and multiplex reduction and its polymer nanocomposites by masterbatch-based melt blending, J. Mater. Chem. 22 (2012) 6088–6096, https://doi.org/10.1039/C2JM16203B.

[18] S. Xiong, W. Wang, G. Fu, J. Hao, P. Liu, Z. Duan, J. Wei, X. Zheng, Graphene quantum dots modified Bi$_2$WO$_6$ with enhanced photocatalytic activity by reinforcing the charge separation, New J. Chem. 44 (2020) 19220–19226, https://doi.org/10.1039/D0NJ03569F.

[19] Y. Liu, B. Wei, L. Xu, H. Gao, M. Zhang, Generation of oxygen vacancy and OH radicals: a comparative study of Bi$_2$WO$_6$ and Bi$_2$WO$_{6-x}$ nanoplates, ChemCatChem 7 (2015) 4076–4084, https://doi.org/10.1002/cctc.201500714.

[20] R. Shi, G. Huang, J. Lin, Y. Zhu, Photocatalytic activity enhancement for Bi$_2$WO$_6$ by fluorine substitution, J. Phys. Chem. C 113 (2009) 19633–19638, https://doi.org/10.1021/jp906680e.

[21] S. Wang, X. Hai, X. Ding, S. Jin, Y. Xiang, P. Wang, B. Jiang, F. Ichihara, M. Oshikiri, X. Meng, Y. Li, W. Matsuda, J. Ma, S. Seki, X. Wang, H. Huang, Y. Wada, H. Chen, J. Ye, Intermolecular cascaded π-conjugation channels for electron delivery powering CO$_2$ photoreduction, Nat. Commun. 11 (2020) 1149–1158, https://doi.org/10.1038/s41467-020-14851-7.

[22] H. Sun, Z. Tian, G. Zhou, J. Zhang, P. Li, Exploring the effects of crystal facet in Bi$_2$WO$_6$/BiOCl heterostructures on photocatalytic properties: a first-principles theoretical study, Appl. Surf. Sci. 469 (2019) 125–134, https://doi.org/10.1016/j.apsusc.2018.11.006.

[23] J. Olowoyo, M. Kumar, S. Jain, S. Shen, Z. Zhou, S. Mao, A. Vorontsov, U. Kumar, Reinforced photocatalytic reduction of CO$_2$ to fuel by efficient S-TiO$_2$: significance of sulfur doping, Int. J. Hydrog. Energy 43 (2018) 17682–17695, https://doi.org/10.1016/j.ijhydene.2018.07.193.

[24] X. Li, J. Song, Y. Liu, H. Zeng, Controlling oxygen vacancies and properties of ZnO, Curr. Appl. Phys. 14 (2014) 521–527, https://doi.org/10.1016/j.cap.2014.01.007.

[25] T. Zhou, J. Hu, J. Li, Er^{3+} doped bismuth molybdate nanosheets with exposed {010} facets and enhanced photocatalytic performance, Appl. Catal. B 110 (2011) 221–230, https://doi.org/10.1016/j.apcatb.2011.09.004.

[26] Q. Wang, G. Wang, X. Liang, X. Dong, X. Zhang, Supporting carbon quantum dots on NH$_2$-MIL-125 for enhanced photocatalytic degradation of organic pollutants under a broad spectrum irradiation, Appl. Surf. Sci. 467–468 (2019) 320–327, https://doi.org/10.1016/j.apsusc.2018.10.165.

[27] E. Karamian, S. Sharifnia, On the general mechanism of photocatalytic reduction of CO$_2$, J. CO$_2$ Util. 16 (2016) 194–203, https://doi.org/10.1016/j.jcou.2016.07.004.

[28] W. Huo, X. Dong, J. Li, M. Liu, X. Liu, Y. Zhang, F. Dong, Synthesis of Bi$_2$WO$_6$ with gradient oxygen vacancies for highly photocatalytic NO oxidation and mechanism study, Chem. Eng. J. 361 (2019) 129–138, https://doi.org/10.1016/j.cej.2018.12.071.

[29] J. Sheng, Y. He, J. Li, C. Yuan, H. Huang, S. Wang, Y. Sun, Z. Wang, F. Dong, Identification of halogen associated active sites on bismuth-based perovskite quantum dots for efficient and selective CO$_2$-to-CO photoreduction, ACS Nano 14 (2020) 13103–13114, https://doi.org/10.1021/acsnano.0c04659.

[30] D. Ješić, D. Jurković, A. Pohar, L. Suhadolnik, B. Likozar, Engineering photocatalytic and photoelectrocatalytic CO$_2$ reduction reactions: mechanisms, intrinsic kinetics, mass transfer resistances, reactors and multi-scale modelling

simulations, Chem. Eng. J. 407 (2021) 126799–126835, https://doi.org/10.1016/j.cej.2020.126799.

[31] X. Li, Y. Sun, J. Xu, Y. Shao, J. Wu, X. Xu, Y. Pan, H. Ju, J. Zhu, Y. Xie, Selective visible-light-driven photocatalytic CO_2 reduction to CH_4 mediated by atomically thin CuIn5S8 layers, Nat. Energy 4 (2019) 690–699, https://doi.org/10.1038/s41560-019-0431-1.

[32] Y. Li, J. Fan, R. Tan, H. Yao, Y. Peng, Q. Liu, Z. Li, Selective photocatalytic reduction of CO_2 to CH_4 modulated by chloride modification on Bi_2WO_6 nanosheets, ACS Appl. Mater. Interfaces 12 (2020) 54507–54516, https://doi.org/10.1021/acsami.0c11551.